1994ApJ...430..800F

THE ASTROPHYSICAL JOURNAL, 430:800–813, 1994 August 1

THE RADIATION GASDYNAMICS OF PLANETARY NEBULAE.
IV. FROM THE OWL TO THE ESKIMO

ADAM FRANK[1] AND GARRELT MELLEMA[2,3]
Received 1993 November 8; accepted 1994 February 1

ABSTRACT

We present the results of two-dimensional radiation-gasdynamic simulations of aspherical planetary nebulae (PNs) evolution. These simulations were constructed using the generalized interacting stellar winds (GISW) scenario of Balick (1987), where a fast, tenuous wind from the central star expands into a toroidal, slow, dense wind. We demonstrate that the GISW model can produce a wide range of aspherical flow patterns. The dependence of the shock morphology on the initial parameters conforms to the expectations of analytical models (Icke 1988). We find that radiative cooling slows the evolution of the forward shock by removing energy from the hot bubble and that radiation heating and cooling changes the temperature structure of the shocked slow-wind material.

We have constructed self-consistent synthetic observations of the models from forbidden line emissivities used in the energy-loss term. We present integrated intensity and long-slit spectrum (position-velocity) maps of the models projected at different angles on the sky. These synthetic observations are compared with real intensity and position-velocity maps of PNs. We find that there is a very good match between the synthetic and real observations in terms of morphologies, kinematics, and physical conditions.

From the results of these simulations we conclude that the GISW scenario can account for most, if not all, PN morphologies, thus confirming Balick's conjecture.

Subject headings: hydrodynamics — planetary nebulae: general — stars: mass loss

1. INTRODUCTION

Planetary nebulae (PNs) take on a diverse range of shapes (Schwarz, Corradi, & Melnick 1993). In the last decade it has been recognized that the morphology of PNs can be accounted for through the interaction of concentric stellar winds. In this "interacting stellar winds" (ISW) model of PNs, a fast tenuous wind from the PNs' central star expands into a slow, dense circumstellar envelope. The envelope was expelled as a wind from the progenitor AGB star (Kwok, Purton, & Fitzgerald 1979). The ISW model has been successful in accounting for many of the observational characteristics of spherical PNs (Schmidt-Vogt & Köppen 1986; Marten & Schönberner 1990; Mellema, 1993, 1994 [Paper III]; Frank 1994 [Paper II]). The majority of PNs do not, however, show spherical symmetry. Instead, most PNs display elliptical or bipolar morphologies (suggesting cylindrical symmetry). Balick (1987) suggested that the shapes of aspherical PNs could be explained through a generalization of the ISW framework. In Balick's scenario the progenitor AGB star expels its slow, dense wind with a toroidal density distribution. The fast wind from the PN central star then drives an outflow pattern which is preferentially aligned with the toroid's symmetry axis. The theoretical consequences of this idea were explored by Kahn & West (1985). By varying the slow wind's equator to pole density ratio (*e/p* ratio), and considering the age of the interacting wind system, Balick conjectured that the full range of elliptical and bipolar morphologies could be recovered with the generalized ISW (GISW) model.

Two-dimensional, analytical models of PNs (Icke 1988; Balick, Preston & Icke 1987; Icke, Preston, & Balick 1989) have successfully demonstrated that elliptical and bipolar outflows can be produced by a GISW model. Numerical simulations of the GISW scenario (Soker & Livio 1989; Mellema, Eulderink, & Icke 1991 [hereafter MEI91]; Icke, Balick, & Frank 1992a, hereafter IBF92) have recovered the analytical results and have shown that the interaction of fast winds and circumstellar toroids produces a rich variety of gasdynamical behavior. In particular, the simulations of MEI91 and IBF92 have shown that the full nonlinear, time-dependent solution of GISW gasdynamics produces flow patterns with features not predicted in analytical models. These features include density enhancements along the poles, fish-tail shaped features extending from the caps of the bipolar flow and well-collimated jets (Icke et al. 1992b). These flow patterns allow the numerical models to embrace both "classical" elliptical and bipolar nebulae (such as NGC 7662 and NGC 6905, respectively) as well as PNs which do not fit into the elliptical or bipolar classifications (e.g., the Red Rectangle and NGC 6369).

While the GISW scenario has had continued success in accounting for the morphologies and kinematics of PNs, the majority of models to date have treated the nebular gas without energy sources or sinks. From observations, however, it is clear that PNs are comprised of gas in different ionization states absorbing energy from the central star and radiating it back into space. Radiation processes can alter the gasdynamic evolution of PNs. One dimensional simulations have already demonstrated the significant role that ionization by the stellar UV flux and cooling from forbidden lines can play in the evolution of PNs. Thus a proper treatment of radiation-driven ionization, heating, and cooling is needed to fully understand the dynamical evolution of PNs (Frank & Mellema 1994, henceforth Paper I). Radiation-gasdynamical calculations also form the critical link between GISW models and observations. The

---

[1] Department of Astronomy, University of Minnesota, Minneapolis, MN 55455.

[2] Sterrewacht Leiden, P.O. Box 9513, Leiden University, 2300 RA Leiden, The Netherlands.

[3] Department of Mathematics, UMIST, P.O. Box 88, Manchester M60 1QD, UK.

1994ApJ...430..800F

calculation of observationally important forbidden and permitted line volume emissivities should be intrinsic to any radiation-gasdynamical model of PNs. These emissivities, if calculated individually as terms in the total radiative cooling, can also be used to produce self-consistent "synthetic observations" of the models. These can be compared with real observations.

After having presented our methodology in Paper I and two types of ISW models in Papers II and III, this fourth paper contains the results of numerical experiments in GISW radiation-gasdynamics. The numerical models we have constructed to perform these simulations incorporate many of the radiation and microphysical processes[4] thought to be important in PNs. The results presented here comprise another step in the numerical study of aspherical PNs evolution. This paper is also intended as a catalog of the generic intensity map morphologies and kinematical patterns (in the optical) which can be obtained with the radiation-gasdynamic GISW model. We have already presented some synthetic intensity maps in Frank et al. (1994). In the next paper in this series, we will explore parameter space more fully in an attempt to constrain models of AGB wind asphericity as well as extend the study of synthetic observations into other wavelength domains such as X-rays.

We note that the results presented in this paper should apply to the formation of bipolar flows in many astrophysical settings. Nebulae surrounding symbiotic stars are thought to be close cousins of PNs and have been modeled analytically with the GISW scenario by Henney & Dyson (1992). Blondin & Lundqvist (1993) have used GISW numerical simulations to model the ring of SN 1987A. Their flow patterns are similar to those of MEI91, IBF92, and those presented here. Another example is the morphology of the Eta Carina nebulae (Meaburn, Wolstencroft, & Walsh 1987). It is quite similar to some bipolar PNs and may have been produced through processes similar to those in the GISW scenario. Bipolar molecular flows and Herbig-Haro jets may also form through a variation of the GISW model (Frank & Noriega-Crespo 1994). Finally, at the largest scales relativistic jets like those seen in AGNs may be driven by GISW-type flows (Eulderink & Mellema 1994). We note that models of wind interactions with stratified external medium have also been invoked to explain galactic superbubbles (MacLow, McCray, & Norman 1989).

The organization of this paper is as follows. In § 2 of the paper we discuss the numerical methodology and initial conditions used in the simulations. In § 3 we present the results of the models in terms of their dynamical evolution. In § 4 we present the synthetic observations derived from the simulations and discuss their relevance to observations of real PNs. In § 5 we provide our conclusions.

2. METHODOLOGY AND INITIAL CONDITIONS

The details and tests of the numerical method used to solve the gasdynamical, radiation, and microphysical equations has been described elsewhere (see references below for the gasdynamical methods and Paper I for the radiation method). We summarize the methodology as follows: we solve the two-dimensional Euler (so no viscosity or heat conduction are included), radiation transfer, and ionization rate equations in axisymmetric, spherical coordinates $[(=r,\ \theta) : v_\phi = 0]$. The gasdynamical equations are solved using either a flux-corrected transport-based scheme (the LCD method of Icke 1991) or a Godunov based Roe-solver scheme (Eulderink 1993; Mellema 1993). Both gasdynamical codes are second-order accurate and can resolve shocks on two or three grid points. The radiation and ionization equations are treated in parallel with the gasdynamics through operator splitting.

Radiation transfer from the central star is treated as a function of wavelength. We consider only the transfer of photons through H and He. Ionization was treated with a time-dependent method for H and He. Ionization equilibrium is assumed for the heavier elements. For temperatures below 10^5 K energy losses through collisonally excited and recombination line radiation is treated as cooling terms in the energy density equation. The forbidden, permitted, and recombination-line energy-loss terms are further resolved into individual lines for various elements (H, He, C, O, N, Ne) and ionization levels (I–V). The emissivities for these lines was calculated using computationally inexpensive fits to full three- and five-level calculations (Balick, Mellema, & Frank 1993). At temperatures above 10^5 K we use the coronal cooling rates of Dalgarno & McCray (1972). We do not include the heating and cooling of dust grains in the energy budget of the models. While dust is expected to be important in young PNs (Zhang & Kwok 1991), limited computational resources have forced us to neglect its influence on the model. We expect, however, that including dust will produce more acceleration and more cooling during the early stages of evolution.

The gasdynamic initial and boundary conditions for the models are the same as those used in MEI91 and IBF92. The fast wind is injected in the first radial row of computational cells. The slow wind begins in the next radial row and continues out to the edge of the grid. The density in the slow wind is assumed to have the following form:

$$\rho(r,\,\theta) = \frac{\rho^*}{F(\theta)}\left(\frac{r_0}{r}\right)^2 , \tag{1}$$

$$F(\theta) = 1 - \alpha\left(\frac{e^{\beta\cos 2\theta - \beta} - 1}{e^{-2\beta} - 1}\right) . \tag{2}$$

In the equations above, r_0 is the radius at which the slow wind begins. The parameter α describes the pole to equator density contrast (q) in the slow wind, e/p ratio $\equiv q = 1/(1-\alpha)$. The parameter β controls the steepness of the poleward decrease in density and, therefore, the shape of the slow wind. Small values of β ($\beta \approx 1$) give almost elliptical density contours similar to those for a disk. Large values of β ($\beta \approx 6$) yield density contours that are nearly spherical with a cone cut near the symmetry axis ($\theta = 0°$). As was discussed in earlier papers the density distribution in equations (1) and (2) represents a toroidal slow wind which as deposited with constant velocity. There is no special reason for using the distribution represented by these equations. We use it as a matter of definiteness and, to some extent, tradition (Icke et al. 1989). We note that in their study of SN 1987A Blondin & Lundqvist (1993) used a number of density distributions as initial conditions including an inverted form of equations (1) and (2). The bipolar flow patterns they show in their results were qualitatively similar to those presented here, in MEI91, and in IBF92.

---

[4] We distinguish between microphysical quantities and gasdynamic macrophysical quantities. Microphysical quantities are those not directly relevant to the gasdynamics (which only feels the heating and cooling). We call optical depths, electron densities, ionization fractions, and gas temperature microphysical quantities.

The initial and boundary conditions for the radiation are as follows: in all the models we present here the central star is assumed to be a blackbody. We chose stellar parameters (surface temperature, T_*, and luminosity, L_*) to ensure that all the gas in the computational grid would be ionized at least to the first stage. For this reason, the choice of stellar parameters may not be representative of the values assumed during the entire lifetime of most PNs. They are, rather, chosen to produce the basic ionization conditions observed in most PNs. For the initial conditions we have chosen the stellar UV flux is able to ionize oxygen up to O^{2+}. The UV flux from the star is continuously injected in the first row of computational cells and is allowed to transfer radially through the grid. We treat the diffuse radiation field through the choice of appropriate recombination coefficients (Osterbrock 1989).

We have run more than 70 simulations with different initial conditions. We have selected five which demonstrate the important generic features of the models' dynamical evolution and observational appearance. The initial conditions for these five simulations are shown in Table 1. The initial conditions are presented as mass-loss rates ($M_\odot$ yr^{-1}), and velocities (km s^{-1}) for fast wind (fw) and slow wind (sw), the α and β values for the slow wind, and the parameters for the central star. The initial density in the slow wind (ρ_*) in equation (1) can be derived from the assumption of a constant wind velocity and conservation of mass,

$$\rho_* = \frac{\dot{M}}{4\pi v_{\rm sw} r_0^2} . \tag{3}$$

All of the runs have the inner boundary set to $r_0 = 1 \times 10^{16}$ cm, a resolution of 100×100 cells on one-fourth of the computational plane ($\theta = 0 - \pi/2$), and a radial cell size of $\Delta r = 2 \times 10^{15}$ cm. Because of the detail included in the radiation part of the numerical method the simulations are computationally expensive. We ended each simulation when the forward shock ran off the grid. Given our initial conditions this comprised between 400 and 1200 yr of simulated evolution and required $\sim$23 hr of Cray-XMP time. We note that all but one of the simulations presented here were computed with the LCD gasdynamical code. Models computed with the Roe-solver gasdynamic code produce nearly identical results (Mellema 1993). We consider this consistency to be an important confirmation of our methodology.

The models presented in this paper incorporate two significant simplifications. First, we consider the fast wind to begin instantaneously after the (equally instantaneous) termination of the slow wind. Second, we hold the energy distribution of the stellar UV flux constant throughout the simulation. Thus our models do not include the evolution of the inner boundary condition for either the fast wind or the central star. These are expected to be coupled (Pauldrach et al. 1988). It is clear that both the evolution of the stellar UV flux and the coupled increase in fast wind velocity will be important factors in determining the dynamics of PNs (Papers II–III; Mellema 1993). In this study, however, we wish to explore the radiation-gasdynamical effects of the GISW scenario in its simplest form. Since an investigation of this kind has not yet been attempted, we believe that it is necessary to understand the consequences of a simple model (with respect to boundary conditions, not physical processes) first. In later papers we will treat the more complicated and uncertain details of time-dependent boundary conditions and their effect on nebular evolution (Mellema 1993). We note that we have not included the effects of heat conduction. The presence of even a small, dynamically insignificant, magnetic field will suppress heat conduction across field lines making its influence of the PNs evolution negligible. Heat conduction can be observationally important for issues relating to X-ray emission (Soker 1994).

We are also limited in these models to rather moderate spatial resolution and short evolutionary times. This is due to the large amounts of CPU times needed for the simulations. Since cooling due to radiation can produce significant compression and collapse of the swept-up slow wind shell, the restriction to moderate resolution constitutes a fundamental limitation of these models. While our simulations clearly resolve the morphologies of the fundamental gasdynamic discontinuitis (e.g., shocks) some details of flow patterns such as instabilities do not appear in these models. We do not contend that we have the resolution needed such that the simulations have converged. We are currently modifying the code to reduce some of the radiation detail and allow faster runtimes with higher resolution. However, in the pesent study we are interested primarily in the evolution and observational appearance of global morphology and kinematic patterns in PNe. Thus the lack of higher resolution does not present a challenge to the results and conclusions presented here. We note that high-resolution GISW simulations with cooling performed by Blondin & Lundqvist (1993) did not show any gross changes in morphology from their lower resolution nonradiative runs.

3. RESULTS: GASDYNAMICAL FLOW PATTERNS

The basic gasdynamical flow pattern associated with the ISW scenario consists of an interaction region formed by a triplet of discontinuities. The interaction region is bounded on the inside and outside by the undisturbed stellar winds. (Weaver et al. 1977; Dyson & Williams 1980). Moving radially outward from the star one first encounters an inner shock where the fast wind (fw) is decelerated, compressed, and thermalized. This thermalization creates a subsonic, high-temperature region downwind of the inner shock. For the fast

TABLE 1

INITIAL CONDITIONS FOR MODEL PN

Model	$M_{\rm fw}$ ($M_\odot$y^{-1})	$V_{\rm fw}$ (km s^{-1})	$\dot{M}_{\rm sw}$ ($M_\odot$ y^{-1})	α	β	T_* (K)	L_* ($L_\odot$)
A	5×10^{-8}	1000	1×10^{-6}	0.5	1	5×10^4	1.14×10^4
B	7×10^{-8}	1000	1×10^{-6}	0.7	2	5×10^4	1.14×10^4
C	1.3×10^{-7}	1000	1.3×10^{-6}	0.8	1	5×10^4	1.14×10^4
D	6.6×10^{-8}	2500	1×10^{-6}	0.7	2	5×10^4	1.14×10^4
E	1×10^{-7}	2000	5×10^{-6}	0.8	7	5×10^4	1.2×10^4

NOTES.—All models have slow wind velocity set to 10 km s^{-1} and temperature set to 200 K. Model E was run on a 70×70 grid with $\Delta r = 3 \times 10^{13}$ cm.

winds considered in the PN problem and pre- and postshock densities are rather low. We refer to the region of high-temperature shocked fast wind as the hot bubble (hb). The low densities and high temperatures in the hot bubble imply cooling times longer than the evolutionary timescale for most PNs. Thus the hot bubble will not be able to cool significantly during the PN's lifetime. At the outer edge of the interaction region is a forward shock. This shock wave is driven into the undisturbed slow wind by the thermal pressure of the hot bubble. Slow-wind (sw) material which passes through the forward shock is compressed and heated forming a dense shell (ds). Unlike the material in the hot bubble, the cooling timescale for the dense shell is short compared to the evolutionary timescale of the PN. Thus when radiation losses are included the shocked slow-wind material quickly radiates away its newly acquired thermal energy. The radiation losses make the forward shock isothermal, ($T_{\rm ds} = T_{\rm sw}$), and produces further compression in the shell. Separating the dense shell of shocked, swept-up slow-wind material and the hot bubble of shocked fast-wind material is the third gasdynamic discontinuity which is a contact discontinuity (cd). Material cannot diffuse across the cd and mixing can only occur via two- or three-dimensional motions (e.g., instabilities, turbulence, etc.)

With this sketch in mind we present in Figure 1 gray-scale representations of the logarithm of gas density for the four models A, B, C, and D. The models are shown at six different times in their evolution. Notice first that the basic triple discontinuity is apparent in each of the models. Consider the final evolutionary frame for each of the models. The forward shock and dense shell appear as the darkest gray-scales. Typical densities are $\langle n_{\rm ds} \rangle \approx 10^3$ cm^{-3}, and $\langle n_{\rm hb} \rangle \approx 1$ cm^{-3}. Interior to the inner shock is the freely expanding undisturbed fast wind. In this region the density decreases from its value $\rho_{\rm fw}$ at the inner radius of the grid becoming geometrically diluted as it expands ($\rho \propto \rho_{\rm fw}(r_0/r)^{-2}$).

Figure 1 demonstrates the dependence of model morphology on key initial parameters. In his analytical study of GISW morphologies Icke (1988) derived an expression for the evolution of the forward shock, r_s, using Kompaneets' (1960) formalism:

$$r_s = r_s(t, \theta) , \tag{4a}$$

$$\frac{\partial r_s}{\partial t} = \left\{ A \left[1 + \left(\frac{1}{r_s} \frac{\partial r_s}{\partial \theta} \right) \right] \right\}^{1/2} , \tag{4b}$$

$$A = \frac{\gamma + 1}{2} \frac{P_{\rm hb}}{\rho_{\rm sw}(\theta)} , \tag{4c}$$

Icke demonstrated that the evolution of the forward shock was controlled by the "acceleration parameter" A, which is the local ratio of driving force for the shock to the external inertia ($P_{\rm hb}$ is the pressure in the hot bubble). In our study we confirm the expectations of Icke's model. The e/p ratio q, the initial shape of the slow wind (β), and the fast wind kinetic energy

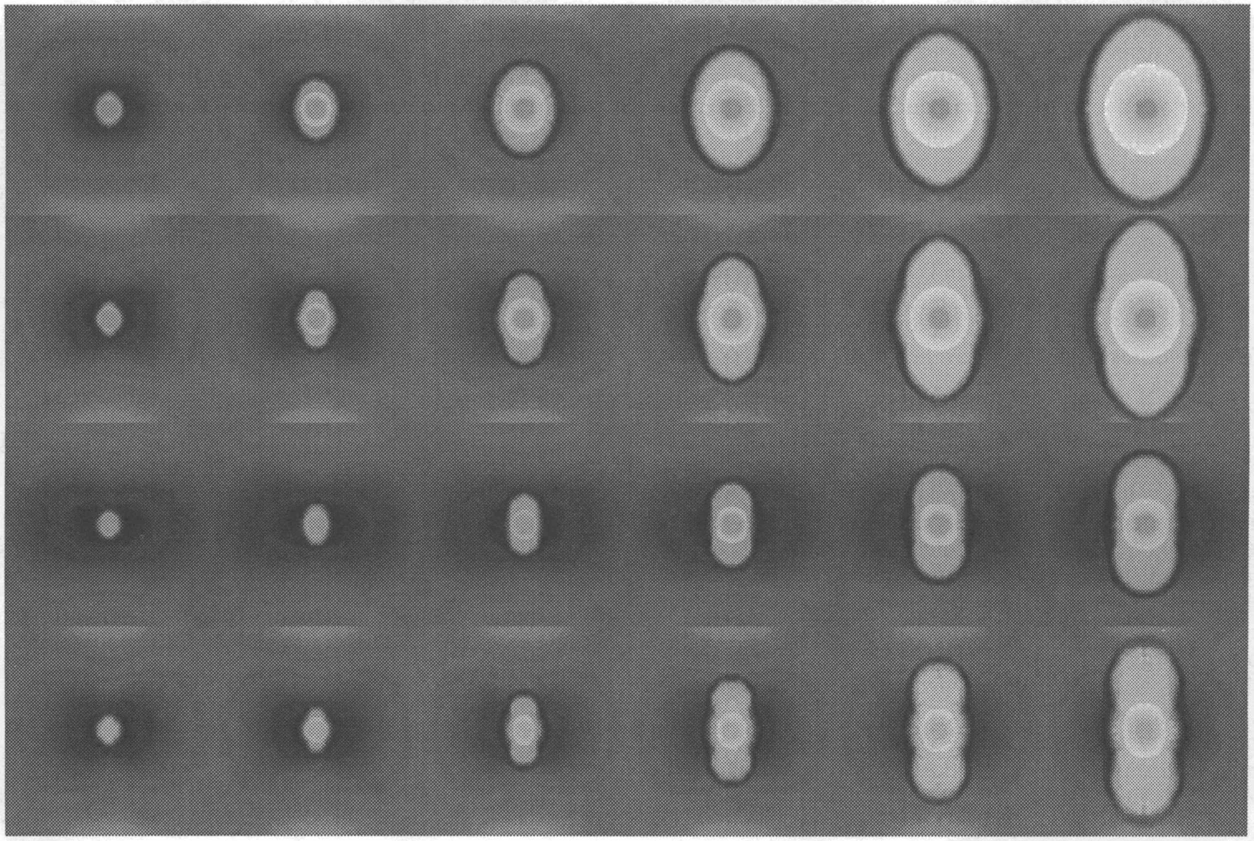

FIG. 1.—Evolution of the density for models A, B, C, and D. Gray-scale representations of $\log_{10}$ are shown at six different times for each model. The final frame for models A, B, and C represent $t = 783$ yr of evolution. The final frame for model D represents $t = 350$ yr of evolution. In the final frame for all the models the darkest gray-scale represents $\log_{10}[\rho({\rm g\ cm^{-3}})] = -20.19$. The lightest gray scales represent $\log_{10}[\rho({\rm g\ cm^{-3}})] = -23.88$. The linear scale of each figure is 4×10^{17} cm square. Note the shape of the inner shock in the different models.

density $e_k = \frac{1}{2}\rho v_{\rm fw}^2$ determine the dynamical shape of both the inner and outer shocks. These are the parameters which also determine Icke's acceleration parameter A. The e/p ratio (through α) and the parameter β are needed to determine the initial slow wind density distribution $F(\theta)$ (eqs. [1] and [2]). In addition $P_{\rm hb}$ is equivalent to the fast-wind energy density e_k. We now consider the role of these input parameters on the shock morphology seen in the numerical simulations.

We examine first the role of the pole to equator density contrast. Model A with $q = 2$ maintains an elliptical morphology throughout its evolution. Models B, C, and D, with $q = 3.33$, 5, and 3.33, respectivly, quickly assume bipolar morphologies which become more pronounced as the models evolve. Here we define bipolar morphology as a forward-shock configuration with one or more cusps separating an equatorial belt (a waist) from the bipolar lobes. From analytical models it can be shown that the cusps represent the intersection of the shock which forms the bipolar lobes with the shock that makes up the equatorial "barrel." We find that $q > 2$ produces bipolar morphologies while $q < 2$ produces elliptical shock configurations. This may be an important point for theories which use common envelope evolution in binary stars (Soker & Livio 1989; Soker & Livio 1989; Soker 1993; Livio 1993) to explain the origin of the slow-wind geometry. The shape of the inner shock depends on the e/p ratio. Note that for $q < 2$ the inner shock is almost is almost spherical while for $q > 2$ it assumes a more aspherical, prolate geometry.

Varying the fast-wind energy density, e_k, changes both the morphology and speed of the models' evolution. Models B and D have the same e/p ratio and β. Model D, however, has a kinetic energy density that is ~ 3 times larger than that in model B. Comparison of their evolution in Figure 1 shows that model D develops a narrower waist band than model B. Model D also evolves faster, expanding off the grid ($r = 2 \times 10^{17}$ cm) in 400 yr compared with 800 yr for model B. Note also that the inner shock is dependent on the fast-wind energy density. The inner shock in model D assumes the most prolate configuration of the models presented here.

The initial shape of the slow wind, determined by β, determines the details of the forward shock morphology such as where the cusps appear. We will see in the next section how this affects the observational appearance of the models.

We note that the morphologies which develop in the radiation-gasdynamic simulations presented here do not differ qualitatively from those produced by the pure gasdynamic simulations of MEI91 or IBF92. We do find that the radiative models evolve with lower forward-shock velocities as was found in one-dimensional spherically symmetric models (Paper I). The velocity of the contact discontinuity, which acts as the piston driving the forward shock, is determined by the pressure in the hot bubble. Thus the difference in the shock velocities between the nonradiative and radiative models can be attributed to the energy lost from the hot bubble. The energy losses in the hot bubble come, primarily from free-free emission. In their GISW simulations Blondin & Lundqvist found a similar result between their radiative and nonradiative models.

In order to complete the description of the dynamical evolution we present in Figures 2 and 3 velocity and temperature maps taken from the models. Figure 2 shows the velocity field in models A and D before the forward shock is driven off the grid. Only those velocity vectors with $|v| < |v_{\rm fw}|$ are plotted. The inner, first row of vectors traces out the inner shock. In model A the inner shock is nearly spherical with only a mild prolate deformation. As was observed in the nonradiative simulations, the weak prolate geometry of the inner shock produces spatial oscillations in the postshock, hot bubble velocity. The origin of this effect is primarily numerical, occurring when the inner shock jumps from one radial row of cells to the next. The inner shock does, however, appear to be subject to a corrugation instability (Landau & Lifshitz 1987) as even high-resolution nonradiative runs show a periodic rippling in the post–inner shock velocity. We conjecture that acoustic noise in the hot bubble, perhaps produced by a ringing mode of the cavity (Frank & Noriega-Crespo 1994), drives local oscillations in the shock normal. These oscillations then cause variations in deceleration through the shock. We note, however, that at the present time the nature of these oscillations remain uncertain and will be the subject of the next paper (Paper V).

Another velocity effect which appears in both the radiative and nonradiative models is flow focusing due to the asphericity of the inner shock. This flow focusing was anticipated by Icke (1988) and was first explored numerically in the GISWs models performed by Soker & Livio (1989). It was later investigated more fully in the higher order accurate models of MEI91 and IBF92. The velocity field for model D is shown in the right panel of Fig. 2. It shows the variation of the shock normal relative to the radially streaming fast wind and the effect this has on the postshock velocity field. When the inner shock is highly prolate the fast wind encounters the shock at an oblique angle. Only the normal component of the fast wind, relative to the shock, will be affected upon passage through the shock. Thus the downstream velocity vector of a parcel of gas will be both shortened and refracted relative to the upstream vector. Given its prolate geometry the inner shock in model D acts as a lens focusing the postshock flow toward the symmetry axis.

In Figure 3 we present a surface plot of the temperature distribution in model C after 783 yr of evolution. The central hole in the temperature distribution marks the freely expanding fast-wind region where temperatures are low ($T \sim 10^4$ K). The "cliff walls" mark the location of the inner shock. The hot bubble dominates the surface plot appearing as the wide peanut-shaped plateau of high temperature. We can estimate the temperature that should be achieved in the hot bubble by using the jump conditions for a strong shock

$$P_2 = \left(\frac{2}{\gamma - 1}\right)\rho_1 v_s^2 , \qquad (5)$$

$$\rho_2 = \left(\frac{\gamma + 1}{\gamma - 1}\right)\rho_1 , \qquad (6)$$

where the subscripts 1 and 2 refer to the preshock and postshock states and v_s is the shock velocity. Observe from Figure 1 that the inner shock is slowly expanding. Thus in the shock frame $v_s \sim v_{fw}$. Combining this fact with equations (5), (6), and the equation of state we conclude that

$$T = \frac{2}{\gamma + 1^2}\frac{m}{k}v_s^2 \sim 3 \times 10^7 \text{ K} . \qquad (7)$$

Figure 3 demonstrates that the temperatures in the hot bubble achieved in the simulations are of this order. Detailed inspection of the temperature distribution in the hot bubble shows, however, that the actual temperatures are slightly lower, an effect which can be ascribed to the slow expansion of the inner shock and the radiative losses in the hot bubble.

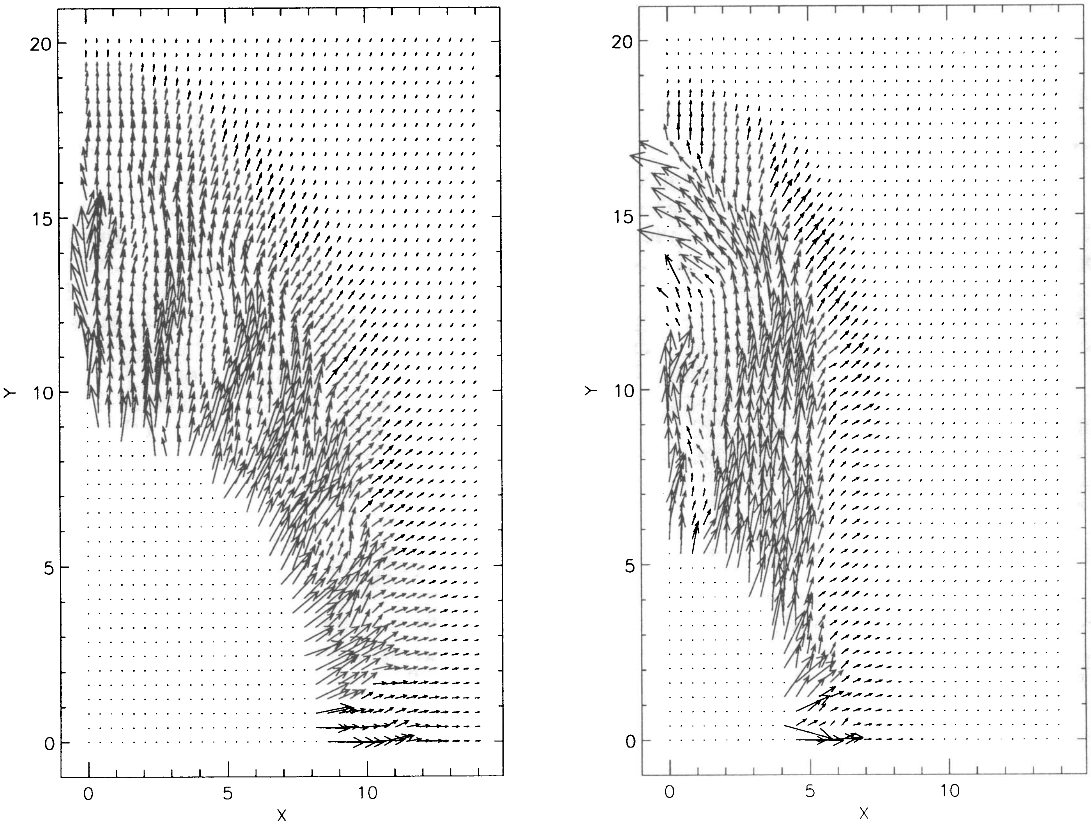

FIG. 2.—Velocity vectors plotted for models A (*left*) and D (*right*) after $t = 783$ and 350 yr, respectively. For model A all velocities less than 1000 km s^{-1} are plotted. For model D only velocities less than 2500 km s^{-1} are plotted. The *x*- and *y*-axes are plotted in units of 1×10^{16} cm. Note the corrugation of the asphericity of the inner shock its effect on the flow there.

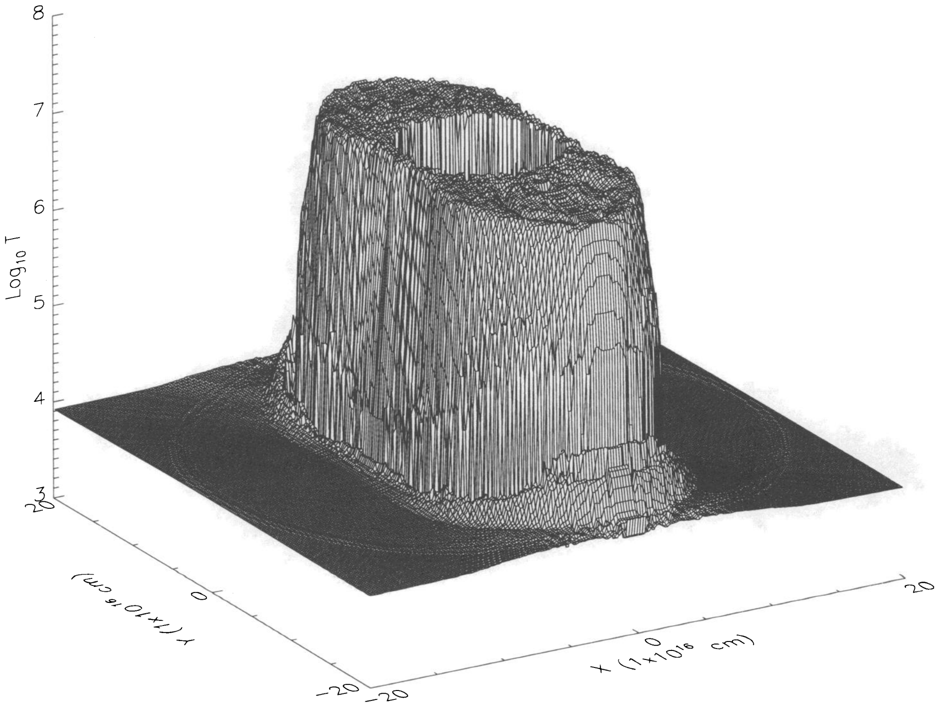

FIG. 3.—Surface plot of $\log_{10}$(temperature) for model C after $t = 783$ yr. The *x*- and *y*-axes are plotted in units of 1×10^{16} cm. Note the high temperatures in the hot bubble and the nearly constant temperatures in the undisturbed slow wind and swept-up shell.

1994ApJ...430..800F

Figure 3 also demonstrates the effect of the stellar UV flux on both the shocked and undisturbed slow wind gas. In our initial conditions $T_{sw} = 200$ K which is appropriate for a cool AGB wind. The UV photons streaming away from the star have ionized and heated the undisturbed slow wind. The ionization also introduces strong collisionally excited forbidden and permitted line cooling into the energy equation. A new thermal balance is obtained at $T_{sw} \sim 9000$ K throughout the undisturbed slow wind. The shocked slow wind in the dense shell also cools effectively. Again the cooling is due to collisionally excited lines, in this case radiating away the thermal energy gained in passing through the forward shock. Figure 3 shows that the forward shock is nearly isothermal. The temperatures in the shell are at most a few thousand degrees higher than that in the undisturbed slow wind. Note that the highest shell temperatures occur at the polar caps. This is to be expected as the densities there are lower and the cooling L, which goes as $L \propto \rho^2$, is less effective.

4. RESULTS: SYNTHETIC OBSERVATIONS

In this section we present projected intensity and position-velocity (long-slit spectra) maps derived from the models. Using the volume emissivities calculated for the total radiative cooling, L, we produce self-consistent synthetic observations of the models. In this section we also discuss the comparison of these synthetic observations with real observations of PNs.

The projected intensity and position-velocity ($P - V$) maps are calculated from the models as follows (see also Henney & Dyson 1992): the two-dimensional volume emissivity $\epsilon(r, \theta)$ from a particular forbidden, permitted, or recombination line is rotated about the symmetry axis to produce a three-dimensional emissivity distribution. This distribution is then mapped on to a Cartesian grid (x, y, z) where the (x, y) plane is considered to be the plane of the sky. The long axis of the model nebulae is placed along the y-axis. The three-dimensional emissivity $\epsilon(x, y, z)$ was then tilted at some angle i with respect to the y-axis and then integrated along the line of sight to form the projected intensity map $I(x, y; i)$. We will refer to i as the inclination angle of the projection. The $P - V$ diagrams were constructed in a similar manner where the tilted emissivity is first binned according to the projected velocity along the line of sight v_l at each point. The $P - V$ diagrams are constructed with the slit set across the long axis of the nebulae ($y = 0$). The true expansion velocity and v_l are then related through, $v_l = v_{exp} \sin i$. The binned emissivities are integrated to give the long-slit spectrum $P - V$ map $S(x, v_l; i)$.

In Figures 4, 6, 8, and 10 we present ($I(x, y, i)$ for the models. In Figures 5, 7, 9, and 11 we present $S(x, v_l; i)$ for the models. The projected intensities and $P - V$ diagrams are calculated using the volume emissivity of the [O III]λ5007 line and are shown at six different inclination angles $i = 12°, 25°, 45°, 60°, 80°$, and 90°. We consider each of the models and its comparison with observations separately. In what follows below we refer to the objects appearing in the synthetic observations as model nebulae.

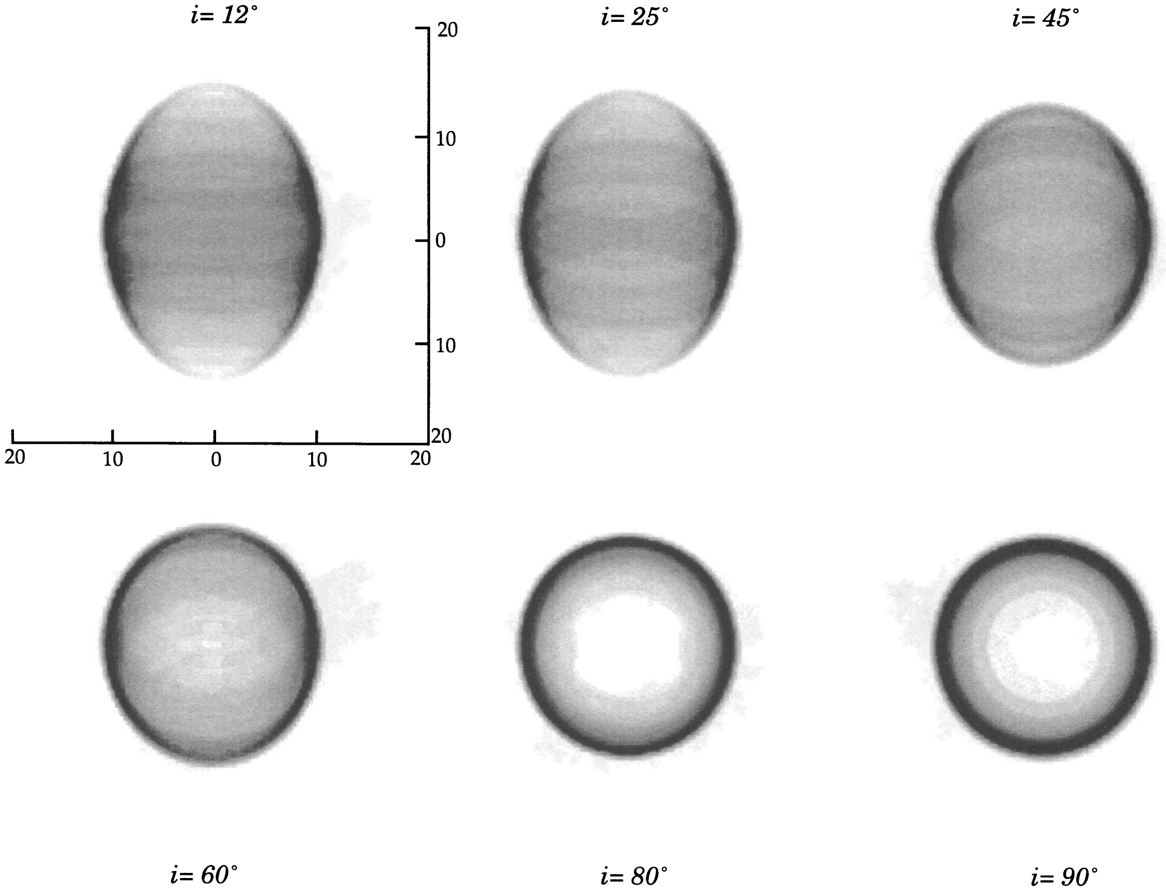

FIG. 4.—Projected [O III]λ5007 intensity map for model A taken after $t = 783$ yr of evolution. the x- and y-axes are plotted in units of 1×10^{16} cm. The projection angle is, from left to right and top to bottom, $i = 12, 25, 45, 60, 80, 90°$. See text for details.

1994ApJ...430..800F

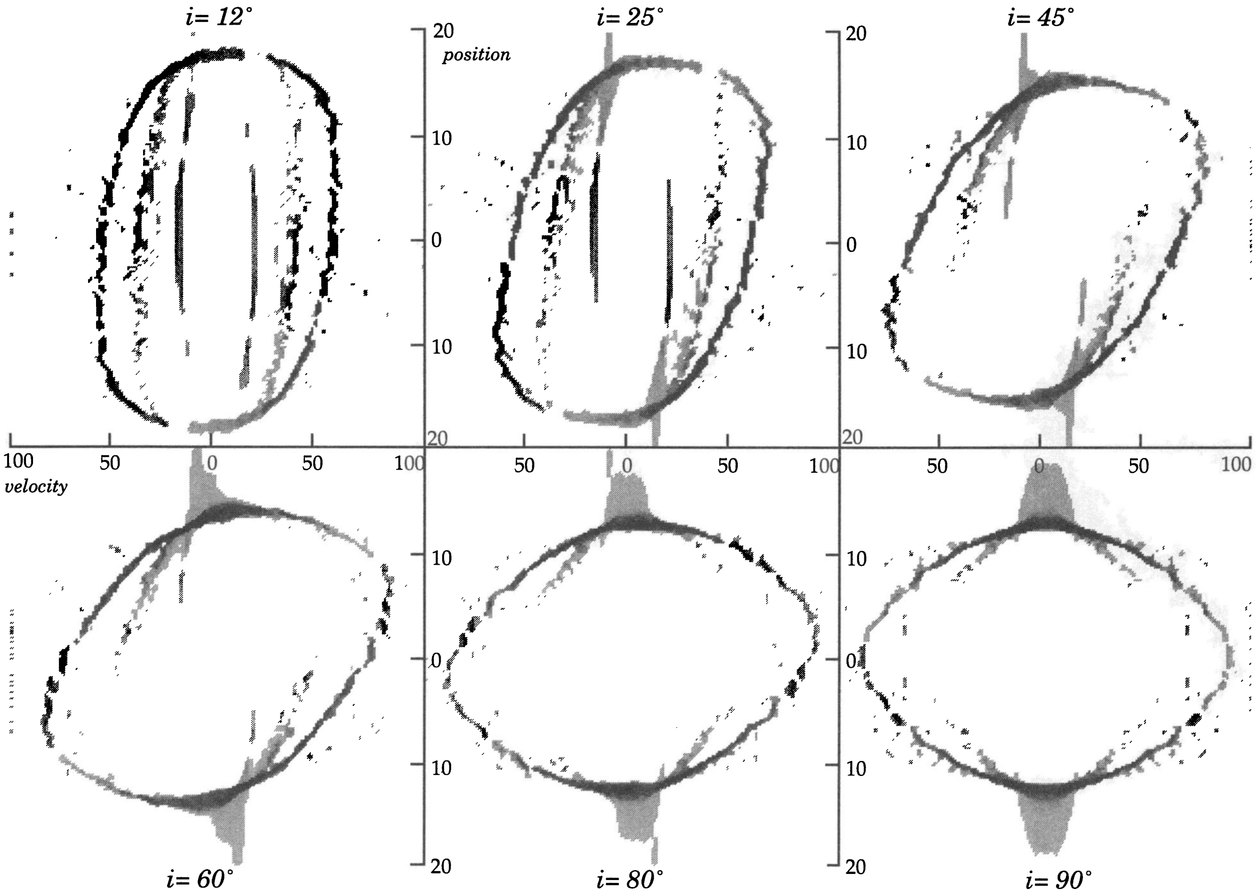

FIG. 5.—Projected [O III]λ5007 long-slit spectrum $P - V$ map for model A taken after $t = 783$ yr of evolution. The position axis is plotted in units of 1×10^{16} cm. The velocity axis is plotted in units of km s^{-1}. The projection angle is, from left to right and top to bottom, $i = 12, 25, 45, 60, 80$, and 90°. See text for details.

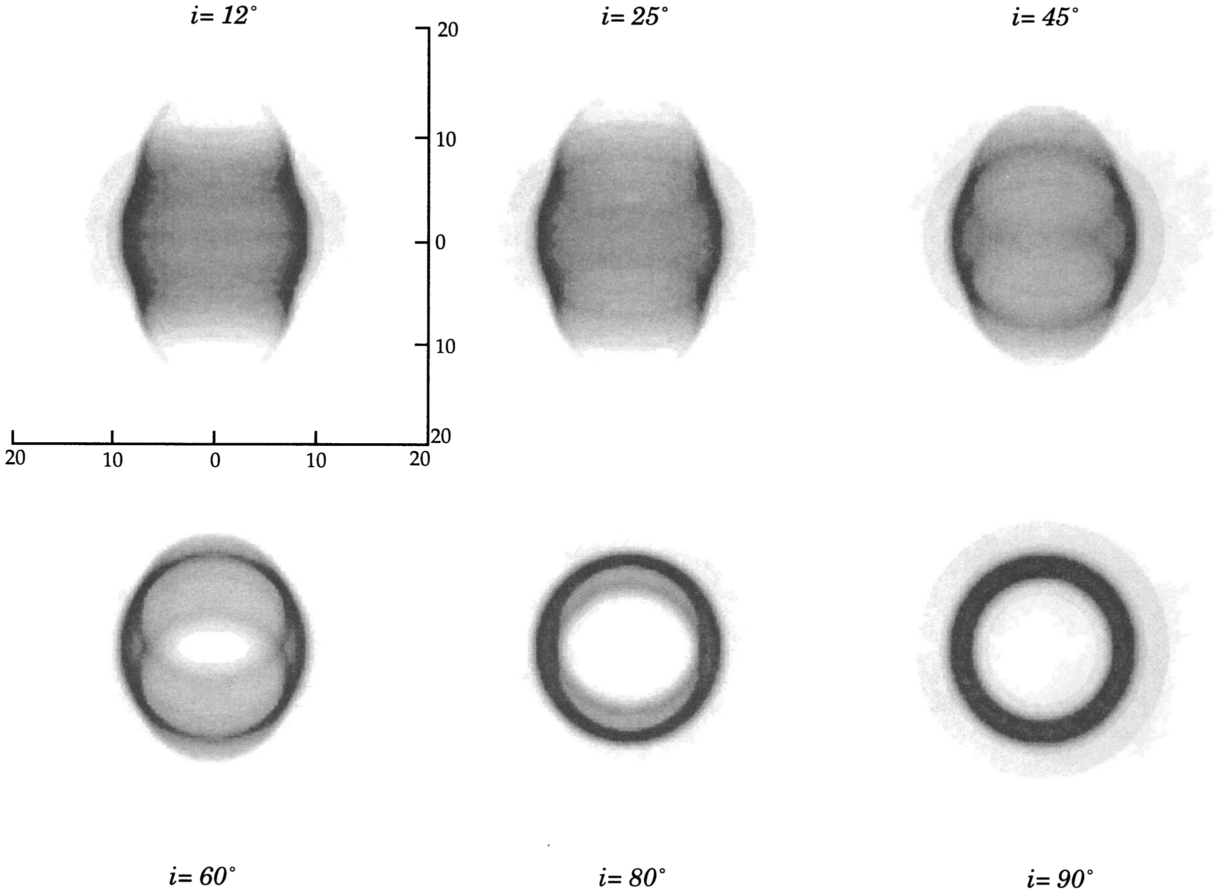

FIG. 6.—Same as Fig. 4 for model B

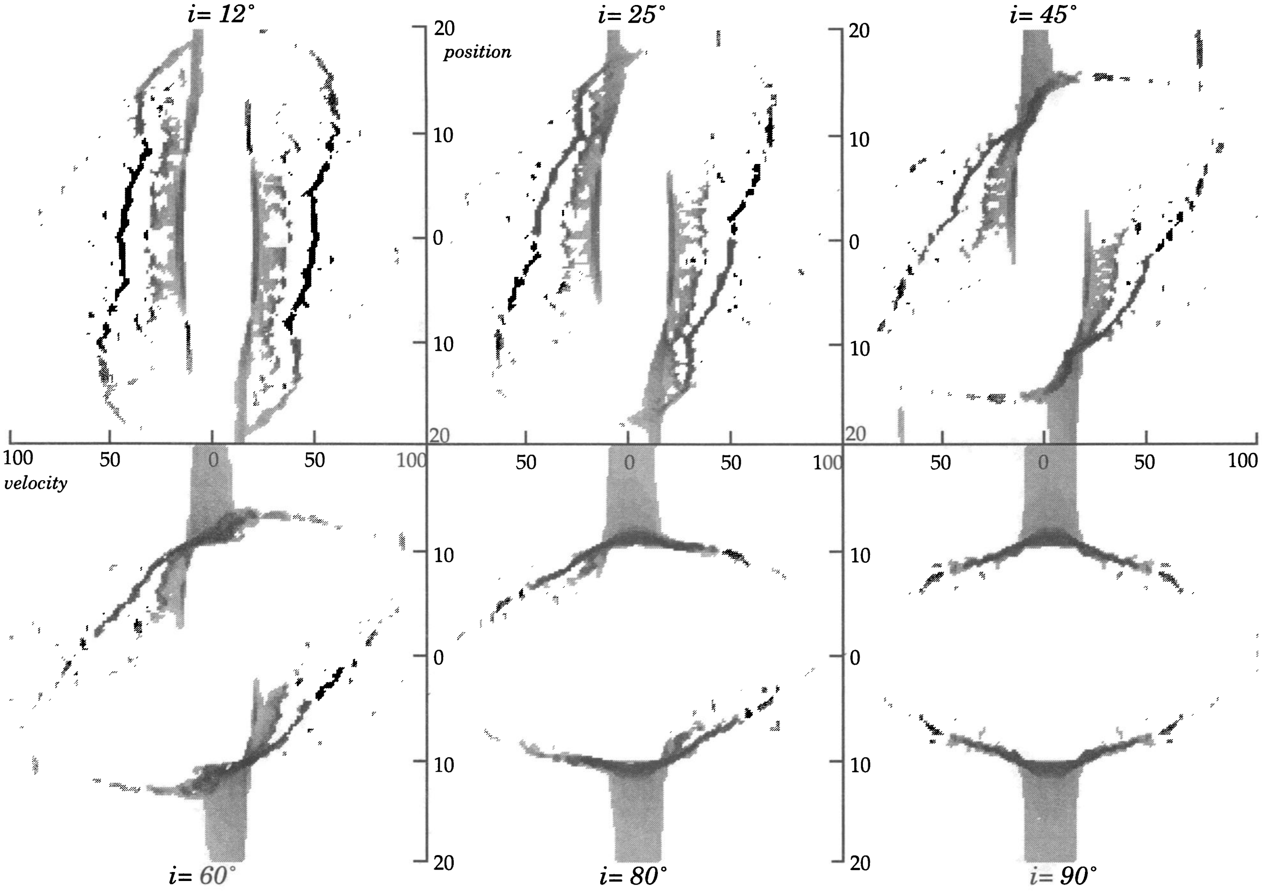

FIG. 7.—Same as Fig. 5 for model B

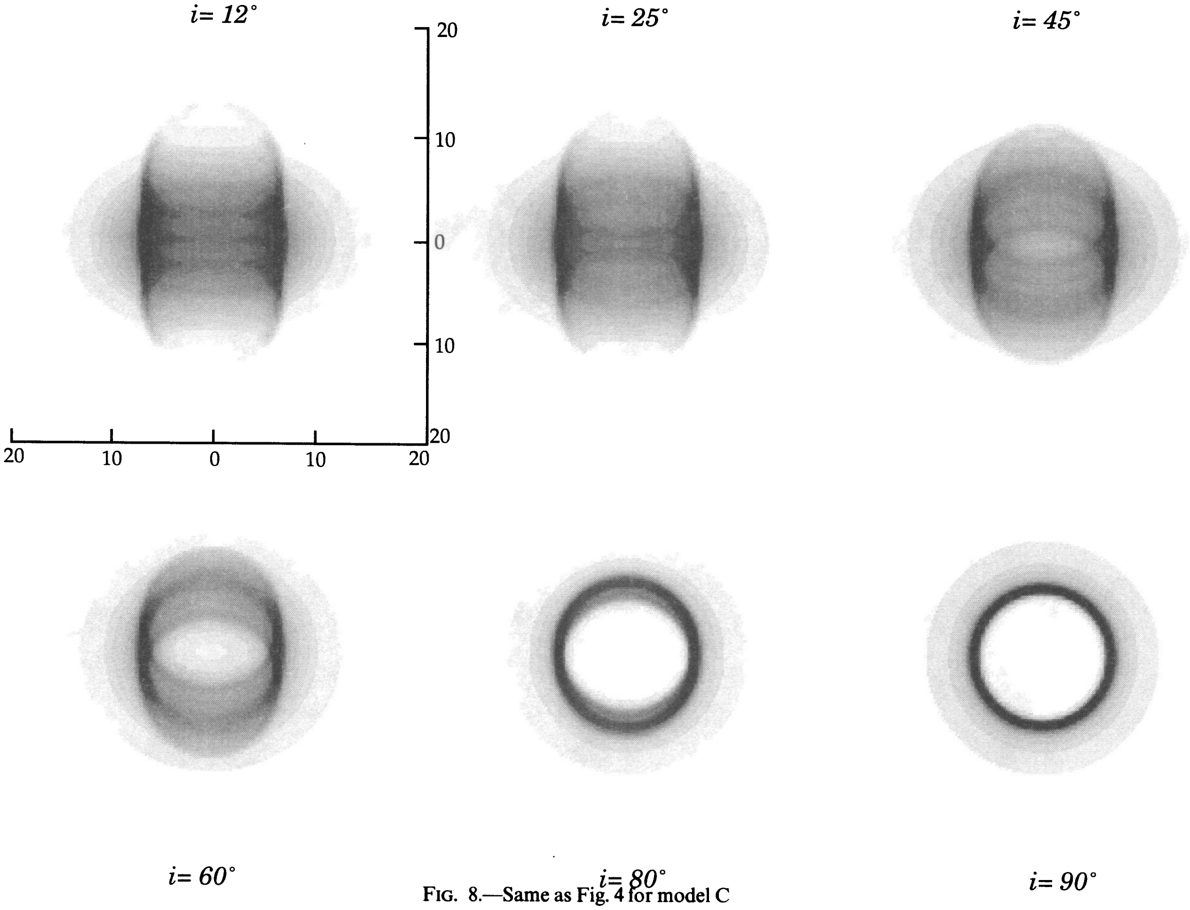

FIG. 8.—Same as Fig. 4 for model C

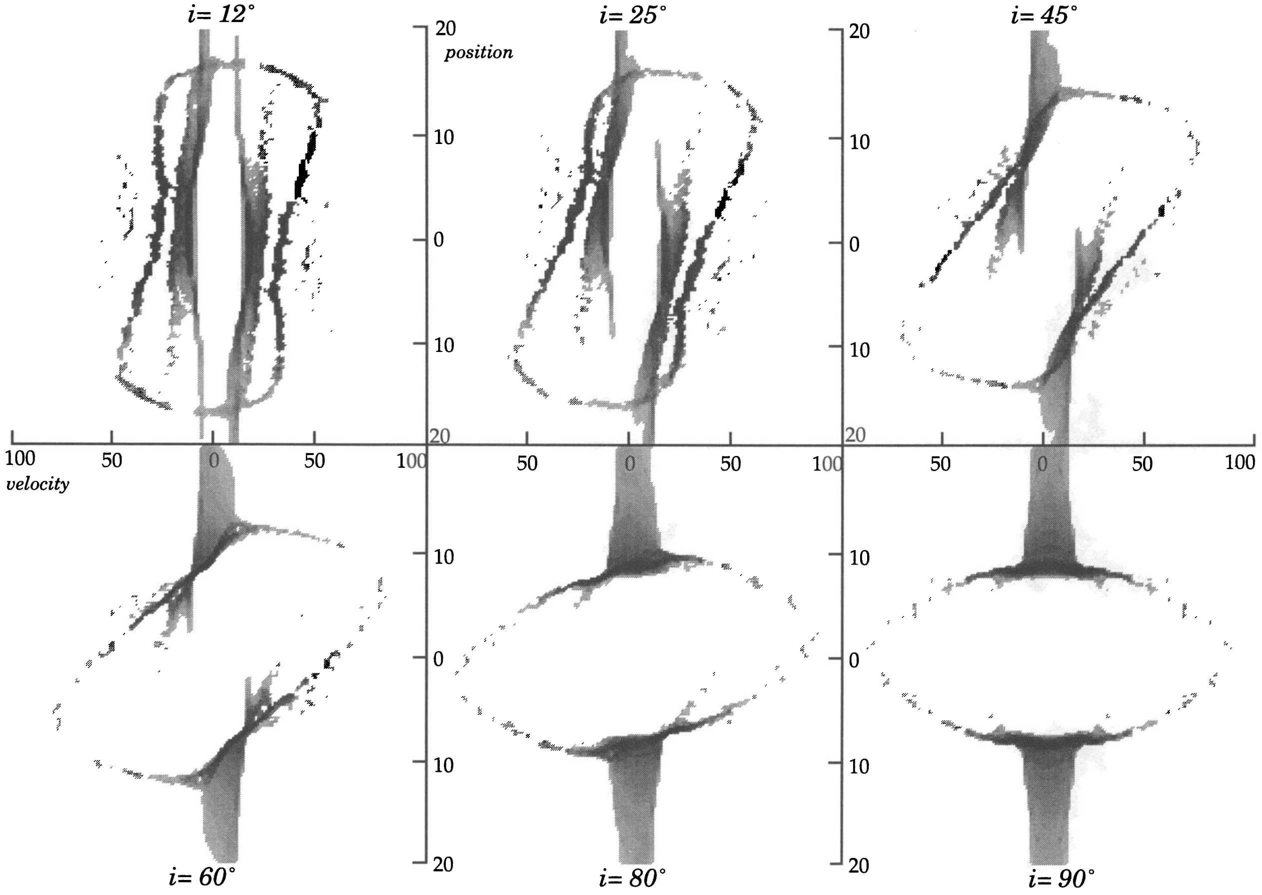

FIG. 9.—Same as Fig. 5 for model C

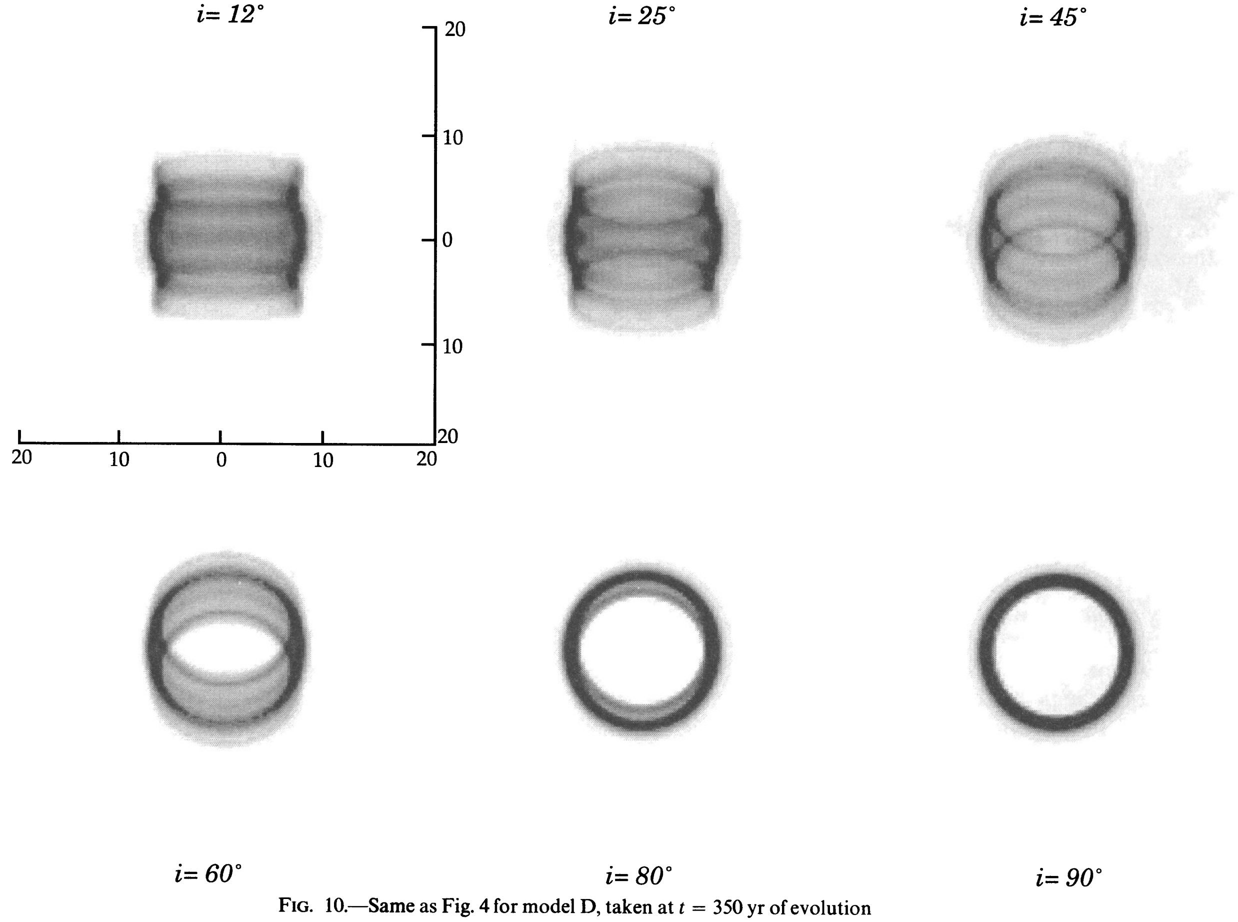

FIG. 10.—Same as Fig. 4 for model D, taken at $t = 350$ yr of evolution

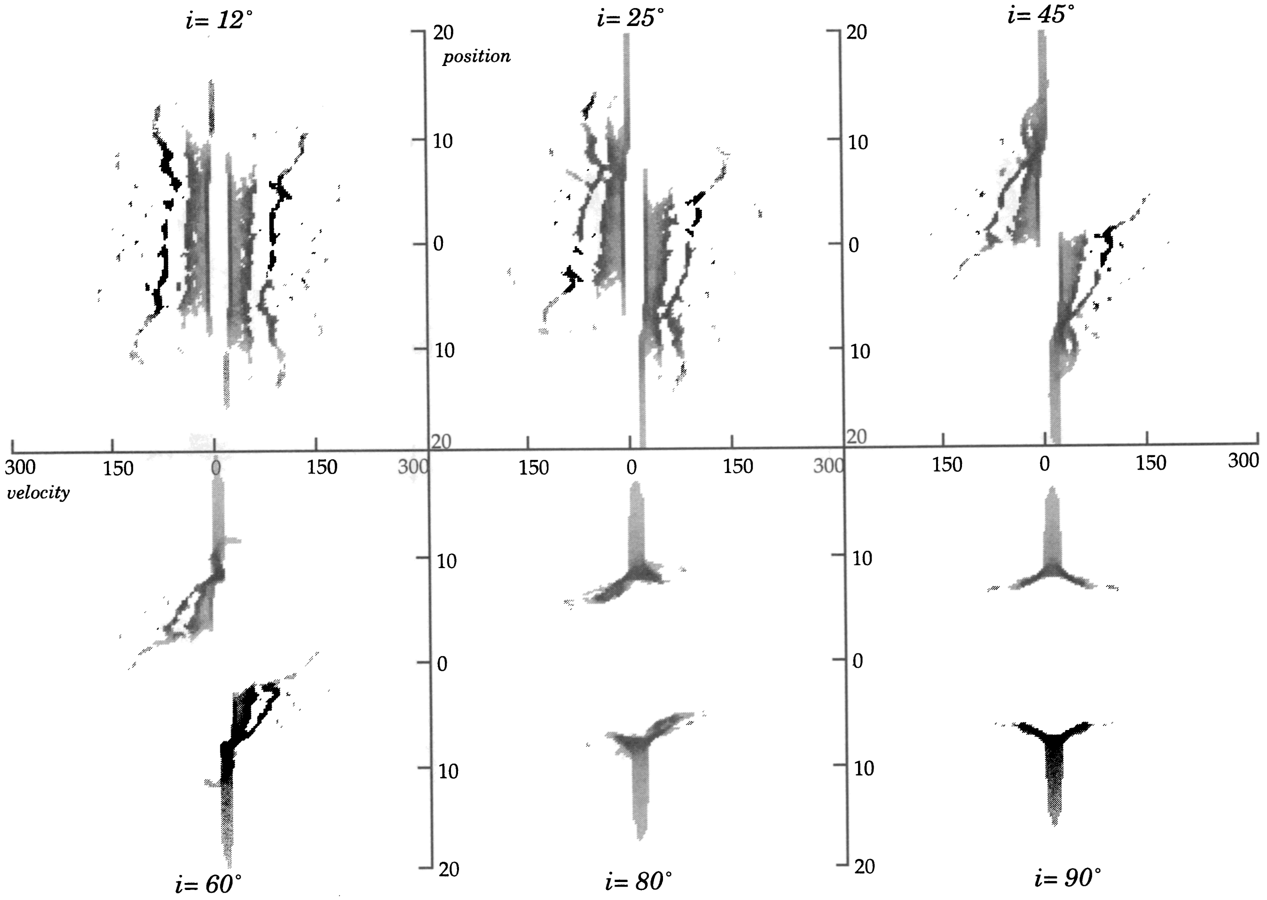

FIG. 11.—Same as Fig. 5 for model D, taken at t = 350 yr of evolution

Figure 4 demonstrates, for model A, the effect of local variations of $\epsilon([\mathrm{O\,III}])$ and projection on the intensity maps. The brightest part of the nebulae appear in the dense shell along the equator where $\epsilon([\mathrm{O\,III}]) \propto \rho^2$ is highest. The nebulae fades near the symmetry axis due to the decreasing density near the poles. At low projection angles the morphology of the model nebulae mirrors that of the density distribution and is essential elliptical. An excellent match to this morphology is seen in M3-9 (Schwarz et al. 1993). For large i, when we look down the pole of the model, the morphology is circular. Note that for $i = 25°$ emission from the front and back of shell intersect forming an hourglass shape across the middle of the model nebulae. This morphology is similar to that seen in the Dumbbell Nebula (NGC 6853). The $P - V$ diagrams for model A shown in Figure 5 indicate that the expansion velocity for equatorial regions of the shell is $v_{\mathrm{exp}} \sim 55$ km s^{-1}. This can be seen from the $P - V$ map at low i. In the $i = 90°$ $P - V$ map the velocity of the shell at the poles is seen to be higher ($v_{\mathrm{exp}} \sim 95$ km s^{-1}). The skewing of the figure as i increases is to be expected (O'Dell & Ball 1985). As the shell is tilted, the higher velocities along the poles are projected onto the line of sight in blue- and redshifted components which skew the kinematic figure. Note that the emission from the slow wind material is seen in the $P - V$ maps both inside and outside the skewed elliptical shell. The slow wind appears skewed up until $i = 90°$. NGC 7662 shows a kinematical pattern (Chu 1989) that is qualitatively similar to that seen in the $P - V$ maps at low i for model A although no slow wind emission internal to the shell appears.

For model B, Figure 6 demonstrates that the cusps in the shell at midlatitudes (coordinate θ) strongly modify the projected intensity maps. Recall that the cusps form where lobe and equatorial shocks meet. The intersection of these shocks produces enhanced densities in the shell. The density enhancements appear as rings in the projected intensity maps. At low i the model nebulae appear as limb-brightened barrels with fainter lobes protruding from the caps. As i increases the rings overlap producing the appearance of eyes in the model nebula. For $i > 60°$ the rings are almost co-extensive and the eyes disappear. With increasing i an ellipse interior to the limb-brightened circular region appears. These patterns are observed in a number of PNs. The general agreement between a simulation with similar initial conditions as model B and observations of PNs morphologies was discussed in Frank et al. (1993); (see their Fig. 2). They found that the morphologies of the projected intensity maps shown in Fig. 6 matched well with (in order of increasing i) NGC 40, NGC 7354, NGC 3587 (the Owl), Abell 82, NGC 2392 (the Eskimo), and NGC 1535. The $P - V$ maps of model B presented in Figure 7 show that the lobes are expanding at high velocities $v_{\mathrm{exp}} \sim 100$ km s^{-1}. In the equatorial regions $v_{\mathrm{exp}} \sim 50$ km s^{-1}. Note that as the inclination becomes very high, $i > 60°$, the kinematical pattern opens up and the dense shell is not continuous. This effect occurs when the line of sight cuts through the throat of a bipolar nebulae exposing high-velocity, low-emissivity gas. Exactly such a pattern is observed in the kinematical studies of the Eskimo Nebula, NGC 2392 (O'Dell & Ball 1985; O'Dell et al. 1990). In those papers the bright shell in the observed $P - V$

map was open with faint, high-velocity "plumes" at positions interior to the shell. The velocity of the shell and plume were calculated to be $v = 60$ and $v \approx 125$ km s^{-1}, respectively. The inclination angle estimated for the Eskimo was $i \sim 70°$. These shell and plume velocities in model B values are in good agreement with these values.

The intensity maps presented in Figure 8 show that model C maintains the appearance of a cylinder up to high inclinations. The overlap of the bright regions near the equator produce elliptical patterns interior to the "walls" of the cylinder. The morphologies shown in Figure 8 are consistent with those seen in A55, IC 4406, He2-36, He 2-64, He 2-141. Mz 1 and Na 2 (Schwarz et al. 1993). The $P - V$ maps for model C presented in Figure 9 show the higher velocities of the lobes relative to the equatorial regions. This can be seen in the hourglass shape of the shell. As the projection angle increases the shell assumes a distribution which is more like a skewed rectangle. In their study of He 2-36, Corradi & Schwarz (1993a) observed a $P - V$ distribution (see their Fig. 2) similar to that seen in Figure 9 for $i = 45°$. In their analysis they concluded that velocities in the nebula range from 45 to 80 km s^{-1} with a projection angle of $i = 30$. They also found that the number densities in the nebulae at the poles are $n = 600$ cm^{-3}. The morphologies shown in Corradi & Schwarz maps, as well as the physical conditions they derive from their observations, are in good qualitative agreement with our model C and synthetic observations derived from it. We note, however, that the appearance of point symmetry in the brightness distribution of the lobes in He 2-36 cannot be explained by our models. We will come back to this point in the last section.

The intensity maps presented in Figure 10 show that, at low inclinations ($i < 45°$), model D assumes a double-horned shape. At higher i the projected intensity assumes the cusp-dominated double-ring "eye" appearance seen in model B. Recall that model D has a high fast wind kinetic energy density. The strength of the wind-wind interaction in this model drives the less dense polar lobes to a high velocity, leaving the shock in the equatorial region behind at smaller radii. Thus the emissivity in the dense, low-latitude, small-radii regions dominates over at the poles. Note that there is significant emission above the cusps which was not seen in model B. Likewise, the rings which form the eyes are brighter in model D than in model B. This double-horned/bright double-ringed configuration has been observed in the symbiotic stars He 2-104, BI Cru, and the planetary nebula MyCn18 by Corradi & Schwarz (1993b), who refer to it as a Crab morphology. The opening angle of the horns can also be thought of as the ratio of the width of the dense shell at the equator to that at middle of the lobes In He 2-104 and BI Cru the opening angle is higher than in Figure 10. We attribute this to differences in age. Our model has evolved for only $t = 330$ yr, while Corradi & Schwarz estimate the age of He 2-104 and BI Cru to be $t \sim 10^3$ yr. The $P - V$ maps for model D are shown in Figure 11. The high expansion velocities in the lobes are apparent at low inclinations. At high i very high velocities show up in the interior of the cavity (as was already discussed for model B). It is important to note that at low i the $P - V$ maps show the lobes flaring out to higher velocities than the equatorial region. By connecting the patterns for the lobes we reproduce the skewed X configuration observed for He 2-104 (Corradi & Schwarz 1993b; Fig. 4). Note that unlike our [O III] $P - V$ map, their kinematic observations were taken in the light of a low-ionization [N II] forbidden line which picks up emission at the poles much like the anomalous FLIERS discussed by Balick et al. (1993b, 1994). These low-ionization knots are not seen in our simulations. The kinematic pattern displayed by the double-ring nebulae MyCn18 (Corradi & Schwarz 1993b; their Fig. 10) shows a skewed column of three ellipses similar to our $i = 45°$ $P - V$ maps for model D. We note, however, that a better match seems to be found in model B at a similar inclination angle.

Finally we present a side by side comparison of real observations and a model. Figure 12 shows the observed [O III]λ5007 image and major axis long-slit spectrum for NGC 3242 (data from Balick [1987] and Chu & Jacoby [private communication], respectively), next to the corresponding synthesized data taken from model E. Model E was calculated using the Roe solver gasdynamic scheme (see § 2). It uses a high value for β (7.0), which leads to the formation of small polar extrusions. Similar extrusions are seen in NGC 3242. We estimate the inclination of this object to be in the range 20°–30°. Therefore the synthesized data are displayed at $i = 25°$. Both the observed and the synthesized $P - V$ diagram have a skewed elliptical shape with a characteristic point symmetry. Note how well the synthesized $P - V$ diagram matches the position of the brightest parts of the spectrum. These correspond to the rings formed by the cusps. NGC 3242 is surrounded by a diffuse outer envelope which shows a higher expansion velocity than the inner bright rim. This is not found in our simplified model. However, simulations in which an evolving star is used do show the formation of such envelopes (Mellema 1993; Paper III). We note that the work of Soker, Zucker, & Balick (1992) provides good data on the initial configuration in the slow wind of NGC 3242. In principle, this data would be better to use as an initial configuration for a model of NGC 3242. However, our purpose in the present paper is to show that the use of a single family of initial conditions can reproduce many of the observed features in real PNs. The use of more realistic initial conditions for detailed comparisons with individual PN will be a future project.

In closing we must note a major deficiency of the models: their inability to produce the fast-moving, low-ionization knots (called ansae or FLIERS) aligned along the major axis of the nebulae (Balick 1993b, 1994). Thus, as discussed in Soker (1990) and verified MEI91 and IBF92, GISW gasdynamics does not appear able to produce ansae in a natural way. The production of ansae remains a mystery which may require the addition of special evolutionary conditions at the early stages of PN formation.

5. SUMMARY AND CONCLUSIONS

5.1. *Summary*

We have presented radiation-gasdynamic simulations of aspherical PN evolution. These simulations were constructed using the GISW scenario where a fast, tenuous outflow from the central star expands into a toroidal, slow, dense circumstellar envelope. We have demonstrated that the GISW model can produce aspherical flow patterns. In particular, we have shown that by varying key initial parameters we can produce a variety of elliptical and bipolar forward shock configurations. The dependence of the shock morphology on the initial parameters conforms to the expectations of analytical models (Icke 1988). We have demonstrated that including radiation-transfer, ionization, and radiative heating and cooling does not drastically

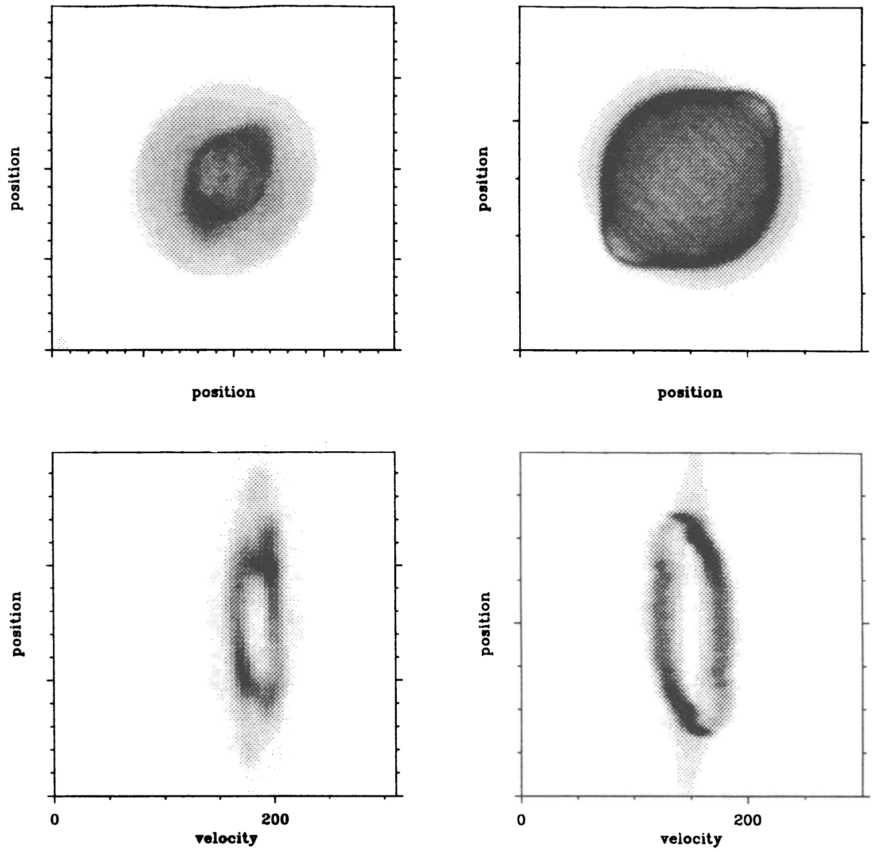

FIG. 12.—Comparison of real and synthesized data. *Top left*: [O III]λ5007 image of NGC 3242 (from Balick 1987). Bottom left: [O III]λ5007 long-slit echelle spectrum along the major axis of NGC 3242 (from Chu & Jacoby, private communication). *Top right*: synthesized [O III]λ5007 intensity map for model E, taken after $t = 1201$ yr. The extent of the x and y axes is 4.5×10^{17} cm, $i = 25°$. *Bottom right*: [O III]λ5007 long-slit spectrum for model E, taken after $t = 1201$ yr of evolution. The position axis extends over 4.5×10^{17} cm, the velocity axis over 300 km s^{-1}, $i = 25°$. The diagram has been smoothed with a Gaussian of 5 km s^{-1} FWHM.

alter the global morphologies. Radiative cooling does slow the evolution of the forward shock by removing energy from the hot bubble. The evolution of the forward shock configuration is independent of the ionization of the undisturbed slow wind. Also, radiation heating and cooling does change the temperature structure of the shocked slow wind material compressed into the dense shell. As is expected for radiative shocks we find $T_{\rm ds} \approx T_{\rm sw}$.

We have also constructed self-consistent synthetic observations of five typical models from forbidden-line emissivities used in the energy loss term. We presented integrated intensity maps and long-slit spectrum ($P - V$) maps of the models projected at different angles on the sky. These synthetic observations were compared with real intensity and $P - V$ maps of PNs. This paper is intended as a survey of radiation-gasdynamic GISW simulation results. Thus in these comparisons we have looked for qualitative agreement between models and reality in terms of morphological and kinematic patterns as well as actual values of physical parameters such as velocities and densities. We find that there is a good match between the synthetic and real observations.

5.2. *Conclusions*

Based on the results presented above we conclude that the GISW scenario proposed by Balick (1987) can explain the majority of PN morphologies and kinematics. While our models contain a number of simplifications with respect to the evolution of the central star and the fast wind it seems clear that the elliptical, barrel shaped, bipolar, double-ring, and owl-eyed patterns seen in many aspherical PNs can be accounted for quite easily through the radiation-gasdynamic version of the GISW model (with projection effects included). The same conclusion holds for the kinematic patterns. The correspondence of the observed $P - V$ map patterns for the Eskimo nebula with the high inclination-angle synthetic observations of models B and D is quite good. This in spite of the fact that the initial conditions for those models were not picked with any particular real PN in mind. Thus while there still remains a number of important questions to be resolved, we feel that the issue of global PN morphologies has been resolved by the GISWs model. *Interacting winds can account for most, if not all, PNs morphologies.* Thus we confirm Balick's original suggestion and the results of earlier nonradiative numerical studies (Soker & Livio 1989; MEI91; IBF92). While it is still possible that other process (such as magnetic fields, Chevalier & Luo 1993) may play a role in shaping PNs it is clear that they are not *needed* to shape PNs.

With respect to PN morphologies three issues stand out which need to be resolved. First, the production of ansae remains an enigma. The solution to this problem appears to require a better understanding of the late stages of AGB star evolution (including binaries and common envelopes; Soker 1993). Second, as was noted before, the question of what effect the evolution of the central star and fast wind have on the evolution of the nebula. To answer this question one of us is currently undertaking computations with time-dependent inner boundary conditions (Mellema 1993). The third question which needs to be addressed is the striking point symmetry which often occurs in PNs (Schwarz et al. 1993). It has been conjectured that point symmetry occurs due to precession of the symmetry axis of the nebulae, something which may be tied to the binary nature of the central source. All of our models are, by assumption, axisymmetric. The synthetic observations, therefore, produce plane- or mirror-symmetric model nebulae. Any departure from axisymmetric geometry requires three-dimensional models which can possibly be numerically simulated with the latest generation of supercomputers. These three-dimensional models will, however, probably need to be nonradiative and low resolution.

Finally, if one accepts our conclusions then the most important question to be asked is not about PNs but about AGB stars: What mechanism produces the dense, toroidal wind at the end of the stars evolution up the AGB? A number of possible mechanisms have been proposed (e.g., rotation, magnetic fields). However, the most promising appears to be gravitational interaction of binary stars either through common envelope evolution or tidal friction (Livio & Soken 1988; Livio 1993; Soker 1993). One of the interesting possibilities that emerges from this paper is the use of PNs morphologies as a diagnostic for theories of AGB wind shaping, in particular the binary star hypotheses. If the GISW model continues to have success in finding accord with observations of PNs then a study of initial slow (AGB) wind parameters, their relation to model PNs morphologies, and the statistics of real PNs morphologies (Stanghellini, Corradi, & Schwarz 1993) may provide constraints for theories of AGB wind shaping. In this way the "What": aspherical PNs, and the "How": GISW radiation gas dynamics might be connected to the "Why": AGB wind shaping.

We wish to thank our advisors B. Balick and V. Icke for the guidance throughout the many years of this project. R. Corradi provided the what, why and how formulation. Y.-H. Chu kindly let us use some of her observations. A. F. wishes to thank A. Noriega-Crespo for his help and Leiden University for its endless hospitality. A. F. enjoyed support from NSF grants AST 89-13639, INT-9200916, AST 91-00486, and the Minnesota Supercomputer Institute. G. M.'s work on PNs was funded by NWO(ASTRON), grant no. 782-372-029.

REFERENCES

Balick, B. 1987, AJ, 94, 671
Balick, B., Mellema, G., & Frank, A. 1993, A&A, 275, 588
Balick, B., Perinotto, M., Maccioni, A., Terzian, Y., & Hajian, A. 1994, ApJ, 424, 800
Balick, B., Preston, H. L., & Icke, V. 1987, AJ, 94, 1641
Balick, B., Rugers, M., Terzian, Y., & Chengalur, J. N. 1993b, ApJ, 411, 778
Blondin, J. M., & Lundqvist, P. 1993, ApJ, 405, 337
Chevalier, R. A., & Luo, D. 1993, preprint
Chu, Y. 1989, in IAU Symp. 131, Planetary Nebulae, ed. S. Torres-Peimbert (Dordrecht: Reidel), 105
Corradi, R. L. M., & Schwarz, H. E. 1993a, A&A, 268, 714
———. 1993b, A&A, 269, 462
Dalgarno, A., & McCray, R. 1972, ARA&A, 10, 375
Dyson, J. E., & Williams, D. A. 1980, Physics of the Interstellar Medium (New York: Wiley)
Eulderink, F. 1993, Ph.D. thesis, Univ. of Leiden
Eulderink, F., & Mellema, G. 1994, A&A, submitted
Frank, A. 1994, AJ, 107, 261 (Paper II)
Frank, A., Balick, B., Icke, V., & Mellema, G. 1993, ApJ, 404, L25
Frank, A., & Mellema, G. 1994, A&A, in press (Paper I)
Frank, A., & Noriega-Crespo, A. 1994, A&A, in press
Henney, W. J., & Dyson, J. E. 1992, A&A, 261, 301
Icke, V. 1988, A&A, 202, 177
———. 1991, A&A, 251, 369
Icke, V., Balick, B., & Frank, A. 1992a, A&A, 253, 224 (IBF92)
Icke, V., Preston, H. L., & Balick, B. 1988, AJ, 97, 462
Icke, V., Mellema, G., Balick, B., Eulderink, F., & Frank, A. 1992b, Nature, 355, 524
Kahn, F. D., & West, K. A. 1985, MNRAS, 212, 837
Kompaneets, A. S. 1960, Dokl. Akad. Nauk SSSR, 130, 1001
Kwok, S., Purton, C. R., & Fitzgerald, P. M. 1978, ApJ, 219, L125
Landau, L. D., & Lifshitz, E. M. 1987, in Course of Theoretical Physics, Vol. VI, Fluid Dynamics (Oxford: Pergamon)
Livio, M. 1993, in IAU Symp. 155, Planetary Nebulae, ed. R. Weinberger & A. Acker (Dordrecht: Kluwer), 279
Livio, M., & Soker, N. 1988, ApJ, 329, 764
MacLow, M. M., McCray, R., & Norman, M. L. 1989, ApJ, 337, 141
Marten, H., & Schönberger, D. 1991, A&A, 248, 590
Meaburn, J., Wolstencroft, R. D., & Walsh, J. R. 1987, A&A, 181, 333
Mellema, G. 1993, Ph.D. thesis, Leiden University
———. 1994, A&A, submitted (Paper III)
Mellema, G., Eulderink, F., & Icke, V. 1991, A&A, 252, 718 (MEI91)
Mellema, G., & Eulderink, F. 1994 A&A, in press
O'Dell, C. R., & Ball, M. E. 1985, ApJ, 289, 526
O'Dell, C. R., Weiner, L., & Chu, Y.-H. 1990, ApJ, 362, 226
Osterbrock, D. E. 1989, Astrophysics of Gaseous Nebulae and Active Galactic Nebulae (Oxford Univ. Press)
Pauldrach, A., Puls, J., Kudritzki, R. P., Méndez, R. H., & Heap, S. R. 1988, A&A, 207, 123
Schmidt-Voigt, M., & Köppen, J. 1987, A&A, 174, 211
Schwarz, H. E., Corradi, R. L. M., & Melnick, J. 1992, A&A, S, 96, 23
Soker, N. 1990, AJ, 99, 1896
———. 1993, in Mass Loss on the AGB and Beyond, ed. H. E. Schwarz (Garching: ESO), 18
———. 1994, AJ, 107, 261
Soker, N., & Livio, M. 1989, ApJ, 339, 268
Soker, N., Zucker, D. B., & Balick, B. 1992, AJ, 104, 2151
Stanghellini, L., Corradi, R. L. M., & Schwarz, H. E. 1993, A&A, 279, 521
Weaver, J., McCray, R., Castor, J., Shapiro, P., & Moore, R. 1977, ApJ, 218, 377
Zhang, G., & Kwok, S. 1991, A&A, 250, 179